



Quantitative analysis of highly efficient PCF-based sensor for early detection of breast cancer cells in THz regime

Sapana Yadav¹ · Pooja Lohia² · D. K. Dwivedi¹

Received: 2 August 2023 / Accepted: 4 September 2023 / Published online: 5 October 2023
© The Author(s), under exclusive licence to The Optical Society of India 2023

Abstract Now a day's breast cancer is a concern in modern science and medicine, consequently establishing an effective and precise breast cancer cell detection approach becomes extremely important. Photonic crystal fiber-based sensor makes this approach smoother and more innovative. A unique THz sensor based on hollow core photonic crystal fiber facilitating chemical analytes detection within terahertz frequency range has been reported in the present work. Efficiency of the presented sensor has been investigated numerically applying simulation technology based on the finite element technique. A photonic crystal fiber biosensor is designed to detect cancerous cells, all the proposed combinations have been implemented by using finite element approach, and the performance of the proposed model has been evaluated by MATLAB software. The reported sensor could be operated in the frequency range 1.0–2.0 THz. Simulation results are found to be good enough, with highly birefringence (0.0020), lower confinement loss (17.33×10^{-9} dB/cm), lower effective area (3.04×10^{-8} μm^2), a higher relative sensitivity (65.53%) along x-axis, relative sensitivity (53.63%) along y-axis, effective refractive index (1.376), nonlinear coefficient (6.38×10^{16}) and dispersion (0.1588 ± 0.0121). Furthermore, the proposed sensor's manufacturing capabilities remain assured by its ease of implementation.

Keywords Confinement loss · Birefringence · THz frequency · Photonic crystal fiber · PbS

Introduction

The development and manufacturing of photonic crystal fiber (PCF)-based sensor have received much attentiveness of numerous researchers across the globe in the current years because of their versatile applications. It has sparked a great deal of interest because of its unique light guiding features and the prospect of light interaction involving gases or liquids. PCF sensor based on PbS has emerged nowadays because of the small size, low price, robustness, the capacity to execute in adverse conditions such as high electromagnetic and chemically exposed fields [1–3]. Sensing of vapor including gases, biochemical sensing, and medicinal analysis, tracking of factory output, ocean and atmospheric research, bio-process control, including automotive control are some of the key characteristics of PCF-based sensors. A. Ramola et al. have reported maximum confinement loss of 40.56 dB/cm at wavelength of 1100 nm for cervical cancer cells using PCF-SPR sensor [4].

Hollow core as biosensor is preferred over the other core types like solid core, as well as porous core since it permits a larger analyte capacity into its core region as measured to other core types. Additionally, since the guided mode in hollow core fibers gets tightly restricted inside the core region, the influence of a background material on the fiber's wave guiding characteristics being effectively decreased [5, 6]. In sensing application, the air inside the air hole core gets replaced by one liquid analyte.

Breast cancer results because of the abnormal growth of breast cells. This illness is highly heterogeneous. Whenever a patient is diagnosed with breast cancer, the breast tissues

✉ D. K. Dwivedi
todkdwivedi@gmail.com

¹ Photonics and Photovoltaic Research Lab (PPRL),
Department of Physics and Material Science, Madan Mohan
Malaviya University of Technology, Gorakhpur 273010,
India

² Department of Electronics and Communication Engineering,
Madan Mohan Malaviya University of Technology,
Gorakhpur 273010, India

take on the shape of a lump, which appears as an aggregation and is usually detected via X-rays [7, 8]. The severity of breast cancer has been reflected in the data on cancer reported in the paper [9]. According to the statistics, Breast cancer is the commonest form of cancer among people between the ages 30 to 39 [10].

Despite breast, cancer has been almost exclusively a female disease, it could also affect men. Breast tumors of any kind are rarely cancerous. The certain growth or swelling in the breast should be examined to see that the cells are cancerous. There are few other methods for testing cancerous tissue, within each variety of attributes [11]. Miller et al. suggested a technique for identifying breast cancer cells using photonic crystal fibers [9, 12]. In recent times, researchers have shown considerable interest in utilizing PCF for biochemical sensing and identification purposes. PCF is a remarkable category of optical fiber that has definite unique features, like optical energy propagation through the PCF having minimum confinement loss (CL) and dispersion having improved nonlinearities [13–15].

Sensitivity and CL are the two vital leading parameters in liquid and chemical analysis. Birefringence would be a primary remarkable feature of PCF, and an increase in its value is foreseen. Asymmetry within fiber [16, 17] could be used to achieve this. PCF with a greater birefringence has been extensively used during telecommunications, chemical detection, and other areas [18–20]. Silica, Teflon, and Zeonex are now just a few forms of fiber materials which could be accepted as bulk materials [18, 19]. Chemical properties of Zeonex have made things exceptionally well enough and distinctive. Various experiments have already shown that Zeonex does have a higher chemical resistance; hence, it is the best fiber material [22, 23].

PCF has been employed to create a wide diversity of chemical and biosensors so far. Arif et al. described another PCF sensor based on PbS [24]. The cladding area with this PbS has hexagonal pattern-oriented air holes; whereas, the core was elliptical. They have reported birefringence as 0.005, the confinement loss as $2.17 \times 10^{12} \text{ cm}^{-1}$ and the sensitivity as 41%. The effective material loss (EML) for the studied sensor has still not been measured [24]. Leon et al. [25] has reported similar as 41%. Its cladding air holes are placed identically to those in the sensor proposed by Arif et al. [24]. Its core is organized into four small circular holes. The sensor has sensitivity approximately 49% and a slightly greater birefringence of around 0.008. Leon et al. have found larger confinement loss, but they have not examined the EML characteristic of the proposed sensor. Hasan et al. in 2019 reported a heptagonal shaped PCF and achieved a sensitivity of 63.24, 61.05, and 60.03% respectively for benzene, ethanol, and water by using TOPAS as a background material. They have suggested alternative PbS having heptagonal organized air holes inside the cladding

area [26]. Sensitivity of the proposed PbS remains slightly greater, about 63.24%. However, the confinement loss and effective area (EA) of the reported sensor were larger.

Hasan et al. [26] have studied a PCF-based chemical sensor in which the cladding holes are heptagonal arranged. At 1.0 THz frequency, the relative sensitivity achieved for the sensor is only 63.24% having low confinement loss. Various optical characteristics of the sensor along with effective material loss (EML) and numerical aperture (NA) have not been evaluated. Yakasai et al. attained 64% relative sensitivity for liquid chemicals (sarin and tabun liquids) in which quad-elliptical core is used [27]. Number of PbS have been reported by other workers [28], but with poor sensitivity, which encourages to explore the possibility to construct a PbS with improved sensitivity, a manufacturing-viable structure, less effective area, birefringence, confinement loss, nonlinearity, and dispersion. Various type of sensors like physical sensors [29, 30], curvature/bend sensors [31], displacement/strain sensors [32], electric and magnetic field sensors [33], pressure sensors [34], temperature sensors [35], torsion/twist sensors [36], transversal loading sensors [37], refractive index sensors [38], vibration sensors [39], multiparameter sensing [40], gas sensors [41], molecular sensors [42], humidity and pH sensors [43] have already been reported in the literature.

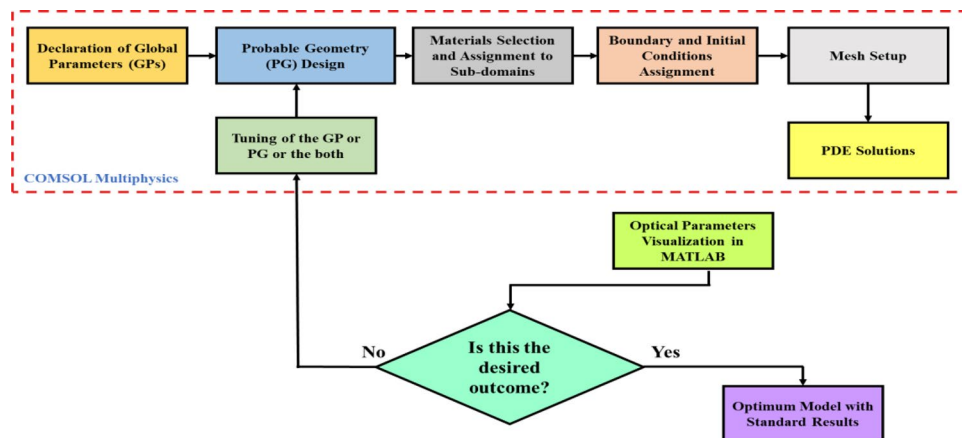
The utilization of a rectangular PCF coupled with Zeonex material in the terahertz regime introduces a range of innovative sensing capabilities. Terahertz waves, being non-ionizing and able to penetrate diverse materials, prove valuable for non-destructive testing, imaging, and sensing in fields such as material characterization, security screening, and medical diagnostics. The distinct sensor design can harness the exceptional features of the rectangular PCF to amplify sensitivity, resolution, or directional sensitivity, specifically tailored for certain applications [44].

The objective of the current work is to implement and evaluate a PbS for identifying cancerous cells. Various parameters have been examined, including relative sensitivity on both the x and y-axis, effective area (EA), confinement loss (CL) and birefringence, effective refractive index, dispersion, nonlinearity, and detection performance. The fabrication possibility of the designed sensor has also been explored. The approach for numerically evaluating the performance of the studied sensor has also been described in detail in Fig. 1. Eventually, the outcomes are provided, with a convincing commentary.

Design of the PCF sensor model

A Photonic crystal fiber (PCF) sensor with a rectangular core and rectangular air holes as the cladding area has been constructed. The sensor is created employing software based

Fig. 1 Diagram illustrates the systematic process of designing and analyzing the sensor model



on finite element technique (FEM). Consecutive steps are considered in the implementation and improvement of models utilizing FEM for the creation of proposed PCF model. Subsequently, both in the core and cladding sections, materials have been allocated. Mesh creation is completed after expressing its initial conditions. Ultimately, performance evaluations get retrieved employing partial differential equation (PDE) algorithms. Parameters such as CL, EA, birefringence, relative sensitivity, dispersion are examined, and the process continue until the desired outcomes are achieved. Figure 2a and b depicts a partial aspect and mesh resolution of the studied sensor. Inside the core area, normal and cancerous cells are used as analytes.

The entire fiber has a radius of 1650 μm . The perfectly matched layer (PML) has a width of 132 μm given the boundary conditions. An electromagnetic signal traveling more toward the surface is intercepted by PML in this case. Twelve rectangular holes surround the cladding; in which air is injected to analysis. The rectangular air holes have the same width (W) as 500 μm , but not the same length. The rectangle core consists of same height and width as 500 μm . R1, R2 and R3 have lengths 500, 2500 and 1500 μm respectively. The separation connecting two holes in the cladding

section is invariable. The pitch (distance joining two adjacent rectangles) of the PCF sensor has been taken 15 μm . The measure joining the centers of two adjacent rectangles has been taken 515 μm . Zeonex has been implemented as fiber substance. In the terahertz band, Zeonex has relatively low absorption loss than few alternative materials like Topas, Silicon, and others. Zeonex is being used to draw metamaterial fibers for the THz region because of its high material loss. Zeonex is worth using as a cladding material but pairing Zeonex with various kinds of different materials allows acquiring the appropriate RI variation to use it as core material. In comparison with Topas, Zeonex has greater chemical resistance and biocompatibility. Zeonex has bulk absorption loss (BAL) 0.2 cm^{-1} in 0.1–10 THz range, with a RI of 1.53 [45]. All over the terahertz spectrum, the above RI maintains a seemingly linear value [13]. A physics-controlled mesh size is employed in the simulation to achieve the most precise results. Complete mesh consists of 68,646 domain elements and 4146 boundary elements of the fiber. The resolution of mesh analysis can be seen in Fig. 2b.

Various articles explain the experimental configuration of sensor applications using PCF-based systems [18, 46–48]. The trial and error method has been used to produce the

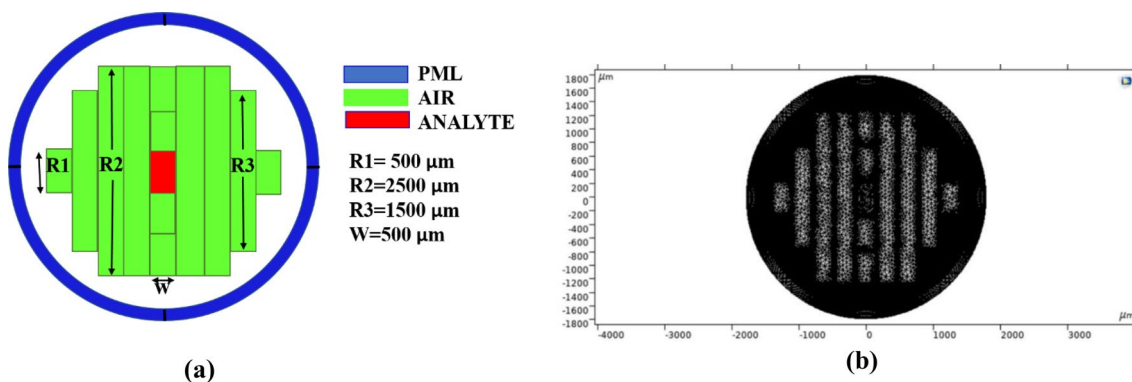


Fig. 2 a Partial representation of the presumed PCF sensor. b An identical Mesh resolution of suggested PCF sensor

structure shown in Fig. 2. This model is selected because of its prevailing outcomes after modeling several designs and comparing its optical properties. This model is referred to as the optimum (OPT) model.

The OPT model has been modified by 2% while keeping the strut value fixed to show a comparability of the optical properties and verify the choice of the OPT model as the recommended sensor in the present paper. Table 1 shows the design parameters for two models that came from the optimization, as well as the OPT model; it contains the width (W) and height (H) of each rectangle.

Cancer cells and normal cells possess light propagation via their analytes inside the x and y directions, as depicted in Fig. 3. Because only a little intensity of light escaped the core region, there was a little loss. The maximum confinement of light is shown in red. As become closer to the core barrier, the intensity starts to fade. The red arrow has indicated the light propagation direction.

Manufacture viabilities

Stacking, sol–gel, 3D printing, and extraction are few of the most familiar techniques of PCF production today. Drilling and slurry casting support sub-micron scale fabrication [49–52]. Circular air holes could be made using the stacking and sol–gel techniques. Extraction and 3D printing techniques, on the other hand, are essential for making asymmetrical PCF sensors, like rectangles. The even and uneven structures contribute to achieving the desired efficiency and used for a variety of sensor applications. Manufacturing of rectangular air holes have already been reported in the literature [50, 53, 54]. Extrusion using fabrication technique could produce executed design of the PCF of the present study.

Fabricating rectangular PCFs can be challenging but achievable through various methods, such as the stack-and-draw technique or the drilling technique. These methods

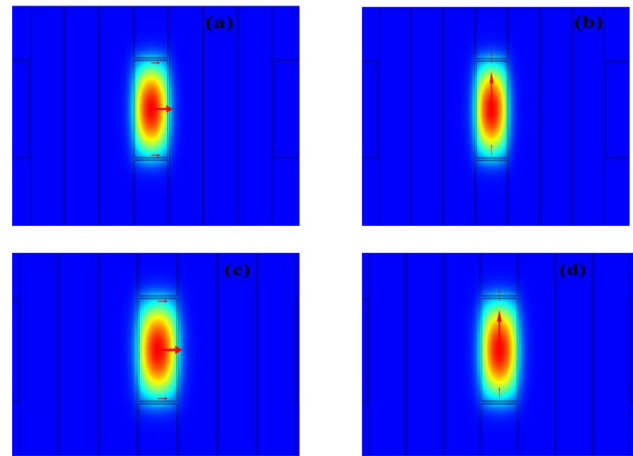


Fig. 3 a and c Mode field distribution along x-polarized light, b and d Mode field distribution along y-polarized light, for normal and cancer cell respectively

involve creating a preform with the desired geometry and then drawing it into a fiber while maintaining the rectangular arrangement of air holes. Specialized equipment and precision control are necessary to ensure the accuracy of the final PCF structure. Once the rectangular PCF is fabricated, it can be integrated into a sensing setup to explore its sensing capabilities. The sensing experiments can be carried out in various ways depending on the specific application. Here are some examples: Chemical Sensing, Temperature Sensing, Strain sensing, Bio sensing, Gas Sensing.

Analytical techniques

The experiment is performed in three separate conditions: OPT –2%, OPT, and OPT +2% for the purpose of an experiment. To achieve these parameters, the width and length of the core are both changed by 2%. The core’s height and

Table 1 Optical characteristics for the studied PCF-based breast cancer cell sensor

Analyte	Model	CL (dB/cm) (y-axis)	EA (μm) × 10 ⁻⁸	Birefringence (B)	RS (x-axis)	Nonlinearity (w ⁻¹ cm ⁻¹) (y)	Dispersion (ps/THz/cm)	N _{eff} (y-axis)
Breast cancer (80%)	Optimum +2%	17.333 × 10 ⁻⁹	3.04	0.00205	65.535%	6.377 × 10 ¹⁶	0.1588 ± 0.0121	1.3769
	Optimum	66.844 × 10 ⁻⁹	3.41	0.02048	24.508%	4.326 × 10 ¹⁶	0.1632 ± 0.0113	.3762
	Optimum –2%	14.544 × 10 ⁻¹⁰	2.81	0.000194	18.245%	4.884 × 10 ¹⁶	0.1660 ± 0.0241	1.3574
Normal cell (30–70%)	Optimum +2%	8.365 × 10 ⁻⁸	2.20	0.00205	60.777%	6.149 × 10 ¹⁶	0.1852 ± 0.0141	1.3630
	Optimum	24.266 × 10 ⁻¹⁰	2.56	0.00233	48.642%	5.580 × 10 ¹⁶	0.1906 ± 0.0215	1.3648
	Optimum –2%	29.5411 × 10 ⁻¹⁰	2.93	0.003023	36.516%	4.934 × 10 ¹⁶	0.2015 ± 0.0540	1.3671

width have been adjusted to 500 and 300 μm respectively, for the best performance. The width has been altered for OPT -2% and OPT $+2\%$ as height remains same as in the optimum case. The width has been set at 294 μm for OPT -2% and 306 μm for OPT $+2\%$.

Initially an analyte liquid is placed in the PCF sensor's core. The refractive index (RI) of material controls the speed of light as it passes through it. It depends entirely on the wavelength of the light inside the liquid analyte as well as the fiber material. Some sensing characteristics, such as birefringence, confinement loss (CL), effective area (EA), effective refractive index, power ratio, relative sensitivity, nonlinearity, and dispersion is used to assess the efficiency of the studied sensor.

Birefringence

Birefringence relates to the inequality in the configuration of the core and the cladding region. This is a fiber material's optical property. Polarization and light propagation have an impact on this optical feature. Birefringence is represented by the RI difference in the two regions, and it is evaluated using following Eq. (1) [55, 56].

$$B = |n_x - n_y| \quad (1)$$

In this context, B represents the birefringence of the polarized mode, whereas n_x and n_y correspond to the actual values of the effective refractive index for x and y -polarization, respectively.

Confinement loss

Confinement loss (CL) arises when the optical confinement of the PCF is lower because of the core-cladding configuration. The quantity of light absorption by the air holes in the cladding around the core is used to evaluate the loss. If the CL were lower, the sensing quality would be improved. CL is denoted by L_{Conf} , and it could be calculated using Eq. (2) [55, 56].

$$L_{\text{conf}} = 8 \cdot 686 \times K_0 \times \text{Img}[n_{\text{effect}}] \times 10^6 \quad (2)$$

Where $K_0 = \frac{2\pi}{\lambda}$, λ represents the wavelength of light and $\text{Img}[n_{\text{effect}}]$ indicates the imaginary value of modal RI.

Effective area

Dependent upon the electric field, light could sometimes travel outside the central region from the analytes. The effective area (EA) is measured as the region where analyte sensing is most efficient. A low EA combined with a substantial

nonlinear effect might lead to high power density in the core region.

Equation (3) allows for the assessment of the EA represented as A_{effect} [55].

$$A_{\text{effect}} = \frac{(\int \int |E|^2 dx dy)^2}{\int \int |E|^4 dx dy} \quad (3)$$

The proposed fiber sensor's electric field distribution is denoted by $|E|$.

Relative sensitivity

The relative sensitivity of a sensor is a crucial characteristic as it signifies the amount of analyte needed to interact with the sensing components. In typical cases, sensing is achieved by adjusting the refractive index (RI). To assess the relative sensitivity (RS), one needs to evaluate the light intensity directly interacting with the sensing analyte [25]. The Eq. (4) is utilized to compute the relative sensitivity (R_s) of the analytes [57].

$$R_s = \frac{n_A}{n_B} P_R \quad (4)$$

The refractive index (RI) of the analyte is represented by n_A ; whereas, the effective modal refractive index is denoted by n_B . Additionally, P_R indicates the power ratio.

Power ratio

The power ratio (P_R) serves as a parameter to quantify the amount of light emitted by the core's sensing materials. Equation (5) can be applied to calculate the power ratio [57].

$$P_R = \frac{\int_{\text{analyte}} \text{Re}(E_x H_y - H_x E_y) dx dy}{\int_{\text{total}} \text{Re}(E_x H_y - H_x E_y) dx dy} \quad (5)$$

The numerator indicates the amount of light transmitted within the core region of the fiber; while, the denominator represents the total cross sectional area. The electric and magnetic field elements are denoted as E_x , E_y , H_x , and H_y , respectively, with subscripts x and y representing the polarizing mode directions.

Effective refractive index

The effective refractive index is the ratio of the speed of light in a vacuum to the speed of light in the medium for a given polarization in the guided design direction (n_{eff}). The Eq. (6) allows one to determine the effective refractive index of any material [58].

$$n_{\text{effpm}} = \left(\frac{c}{v_{zpm}} = \frac{\lambda_0 v}{v \lambda_{zpm}} = \frac{\lambda_0}{\lambda_{zpm}} = \frac{2\pi}{k_0} = \frac{\frac{2\pi}{k_0}}{\frac{2\pi}{K_{zpm}}} = \frac{K_{zpm}}{k_0} = \frac{\beta_{pm}}{k_0} \right) \quad (6)$$

where $K_{zpm} = \beta_{pm}$, p denotes the polarization (TM or TE) and m denotes the mode of the polarization, β_{pm} denotes the propagation constant and $k_0 = \frac{\omega}{c} = \frac{2\pi v}{\lambda_0} = \frac{2\pi}{\lambda_0}$ denotes the number of waves in vacuum, the symbol λ_0 represents the wavelength, and v represents the frequency in a vacuum. By examining Eq. (6), it can deduce that the effective refractive index is dependent on both the frequency and propagation constant.

Nonlinearity

The proportion of light intensity to confine is largely determined by the nonlinear coefficient of the PCF, which is denoted as ‘ γ ’. Nonlinearity is closely related to effective area of the fiber. The nonlinear coefficient can be evaluated by using the Eq. (7) [24].

$$\gamma = \frac{2\pi}{\lambda} \left(\frac{n_2}{A_{\text{effect}}} \right) \quad (7)$$

The nonlinearity of the fiber material is denoted by n_2 , and A_{effect} represents the effective area. The higher level of nonlinearity is accountable for the phenomenon of super-continuum generation (SCG).

Dispersion

The adoption of Zeonex like a fiber material may result in low material dispersion [52]. Consequently, the dispersion may be avoided, and the only dispersion that is the waveguide dispersion must be considered. PCF has the ability to

inherit multichannel transmissions, which could be examined more easily with flat dispersion. As a result, the performance of signal propagation from the transmitter to the receiver can be enhanced. The dispersion (D) of suggested sensor is calculated using the Eq. (8) [56, 58].

$$D = \left[\frac{2}{C} \frac{d\text{neff}}{d\omega} + \frac{\omega}{c} \frac{d^2\text{neff}}{d\omega^2} \right], \text{ (ps/THz/cm)} \quad (8)$$

where ω , c and n_{eff} denote the angular frequency, speed of light and the effective refractive index, respectively.

Results and discussion

A series of information of the proposed biosensor are acquired from finite element method (FEM)-based software for detecting CL characteristic, EA, birefringence and relative sensitivity characteristic along the x and y axes. The operating frequency is 1.8 THz. In the present paper, two sorts of cells: cancerous and normal cells have been identified and examined.

Figure 4a represents the birefringence of cancerous cells while 4(b) shows normal cells’ birefringence. The calculated birefringence is 0.00205, 0.02048, 0.000194 for cancerous cells, and 0.00205, 0.00233, and 0.00302 in case of normal cells for OPT + 2%, OPT and OPT -2% case, respectively.

The birefringence property of the designed biosensor has been calculated and presented in Fig. 4a and b by using Eq. (1). The projected PCF’s birefringence decreases as the working frequency increases, as shown in Fig. 4a and b. With increasing frequency, the index contrast between the polarization modes increases, which results to decrease in birefringence. Zeonex is a transparent thermoplastic material commonly used in various optical applications due to its excellent optical properties and low birefringence. Unlike

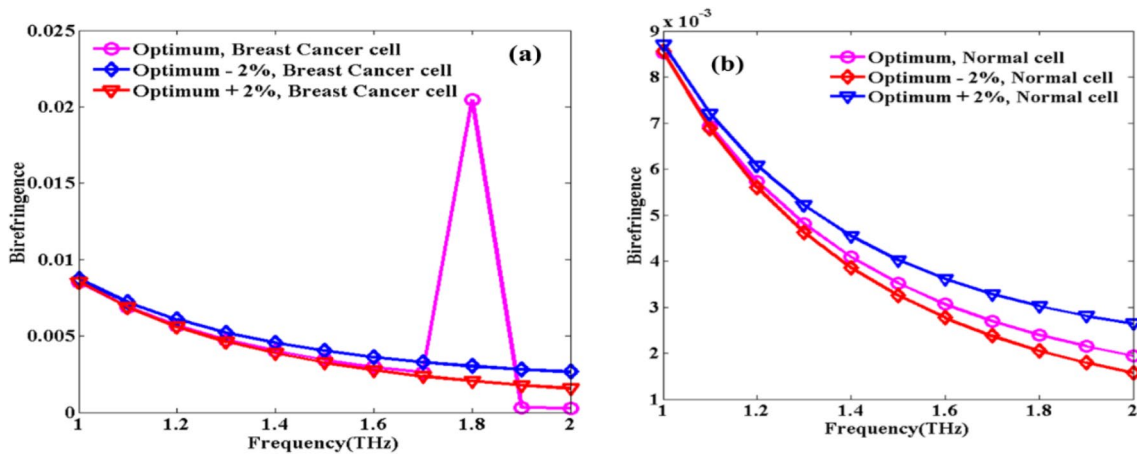


Fig. 4 a Birefringence plot of Breast cancer cells and b Normal cells

most anisotropic materials, Zeonex has a negligible intrinsic birefringence, which means that its refractive indices for the two orthogonal polarization components are very close to each other across a wide range of frequencies. The reason behind Zeonex's low birefringence lies in its molecular structure. Zeonex is designed to be optically isotropic, meaning that its molecules are arranged randomly without any preferred direction or alignment. As a result, the refractive indices of Zeonex do not significantly vary with the direction of light polarization, leading to minimal birefringence.

Similarly, Fig. 5a, b and c, d represents the cancerous cells' confinement loss plot and normal cells' confinement loss plot in x and y-direction, respectively. The cancerous cells' confinement loss values are 17.3328×10^{-9} , 66.844×10^{-9} , and 14.5444×10^{-10} and normal cells' confinement loss values are 8.3649×10^{-8} , 24.26592×10^{-10} , and 29.5411×10^{-10} for OPT + 2%, OPT % and OPT - 2% case, respectively.

The optically confined result, as well as a part of the designed PCF structure, can be seen in Fig. 5a, b and c, d. The smaller the confinement loss (CL), the higher the optical confinement into the PCF's core region. Light confinement within the core region greatly enhances if air holes occur in the cladding region of PCF. If an infinite number of air holes are deployed in PCF, the CL must be zero, as per the mathematical framework. Numerical air holes were required in real-world applications, and therefore appear to be simple to generate inside a PCF.

From Fig. 5, it is observed that a rise in frequency reduces confinement loss because wavelengths are lowered as frequency increases, and all these relatively small wavelengths are more concisely confined within the core. It can be concluded that y-polarization suffers less loss than x-polarization, which could be attributed to the fact that y-polarization strongly confining more light in the core area than x-polarization [24].

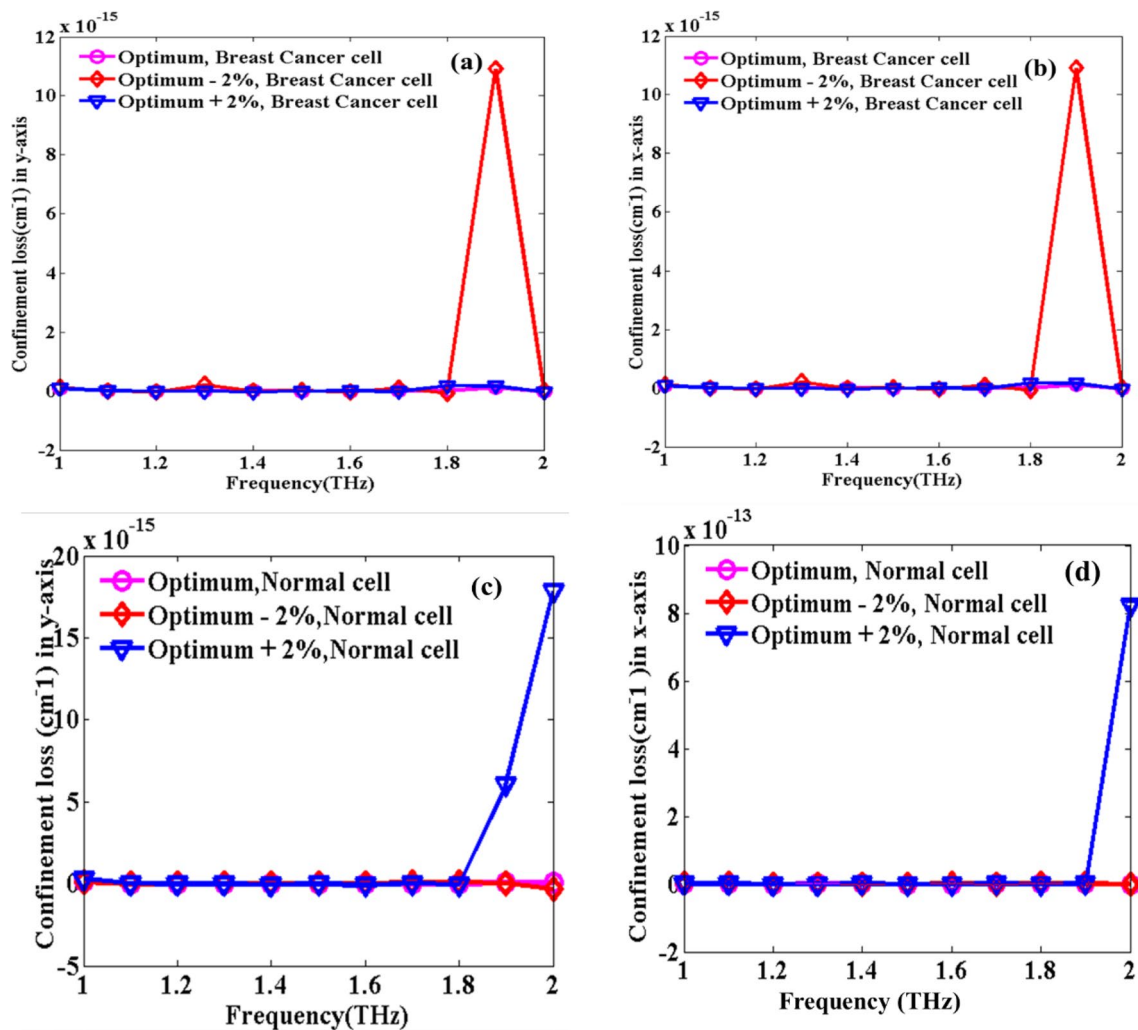


Fig. 5 a and b Confinement loss in breast cancer cell in x and y-axis and c and d normal cell in x and y-axis

Figure 6a represents the cancerous cells' effective area and (b) depicts normal cells' effective area. The cancerous cells' effective areas are $3.04 \times 10^{-8} \mu\text{m}^2$, $3.41 \times 10^{-8} \mu\text{m}^2$, and $2.81 \times 10^{-8} \mu\text{m}^2$ and normal cells' effective areas are $2.20 \times 10^{-8} \mu\text{m}^2$, $2.56 \times 10^{-8} \mu\text{m}^2$, and $2.93 \times 10^{-8} \mu\text{m}^2$ for OPT +2%, OPT and OPT -2% case respectively.

Effective area decreases with increasing frequency for cancerous cell at different OPT +2%, OPT, OPT -2%. Similarly, the effective area of normal cell decreases with increasing frequency for cancerous cell at different OPT +2%, OPT, OPT -2%.

The variation beta frequency and effective area of the studied PCF can be seen in Fig. 6a and b. Effective area of the studied PCF with analyte reduces almost linearly with a rise in operating frequency, as shown in Fig. 6a and b. At 1.8 THz, the photonic crystal fiber experiences a transition from one band gap to another (a change in the mode profile due to a shift in the photonic band structure). This leads to a sudden reduction in the effective area as the guided mode becomes more confined.

Fundamentally, the effective area of a PCF in the transverse dimension is the proportion of cross sectional area it covers. The electric fields in the fiber have determined effective area, which decreases as frequency increases. At lower frequencies (longer wavelengths), the photonic crystal lattice structure can effectively confine light to a smaller region, resulting in a smaller effective area. This occurs because longer wavelengths allow light to interact more strongly with the periodic structure, leading to enhanced mode confinement.

Conversely, at higher frequencies (shorter wavelengths), the photonic crystal lattice may become less effective at confining light, leading to a larger effective area. In other words, as the wavelength decreases, light tends to spread out over a

larger area, reducing mode confinement and thus increasing the effective area.

Figure 7a, b and c, d describes the effective RI of cancerous cells and normal cells, respectively. The effective refractive indices (n_{eff}) of cancerous cells are 0.89995, 0.88728, and 0.89950. Normal cells' effective refractive indices are 0.89205, 0.89087, and 0.89356 for OPT +2%, OPT and OPT -2% case correlatively.

Figure 7a, b, c, and d describes the alteration between the frequency and effective refractive index. The air holes of core in the proposed PCF are asymmetric in design, resulting into a considerable variation in refractive index between the polarization modes and therefore attaining high birefringence. With the progressive increase in frequency, it has been observed that the variation in effective RI is finite, and this property of the studied fiber gives very low dispersion.

For light signals with a range of frequencies, the effective refractive index is a weighted average of the refractive indices corresponding to those frequencies. Since higher-frequency light tends to experience a higher refractive index, it can contribute more to the effective refractive index, resulting in an increase in the effective refractive index with increasing frequency.

Figure 7a and b depicts that the effective refractive index (n_{eff}) rises with rising frequency for cancerous cell. From Fig. 7c and d, it is evident that the effective RI increases as the frequency increases, which could be because a higher frequency (lower wavelength) electromagnetic signal chooses to pass through a higher refractive index region. At 1.8 THz, the photonic crystal fiber experiences a significant change in its photonic band structure, leading to a sharp change in the effective refractive index. This is due to the alignment of certain periodicities in the PCF structure with the wavelength of light at that specific frequency.

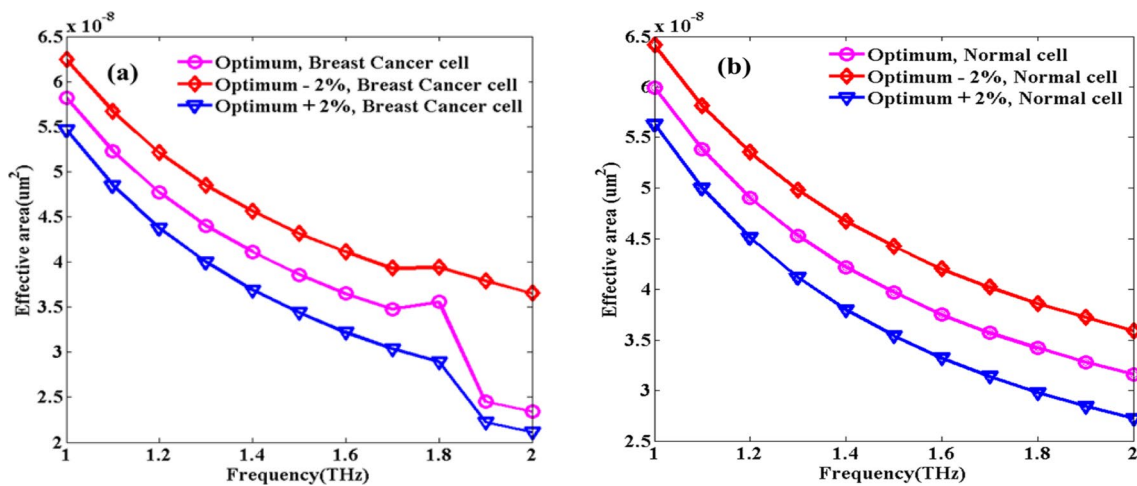


Fig. 6 a Effective area in breast cancer cell and b normal cell

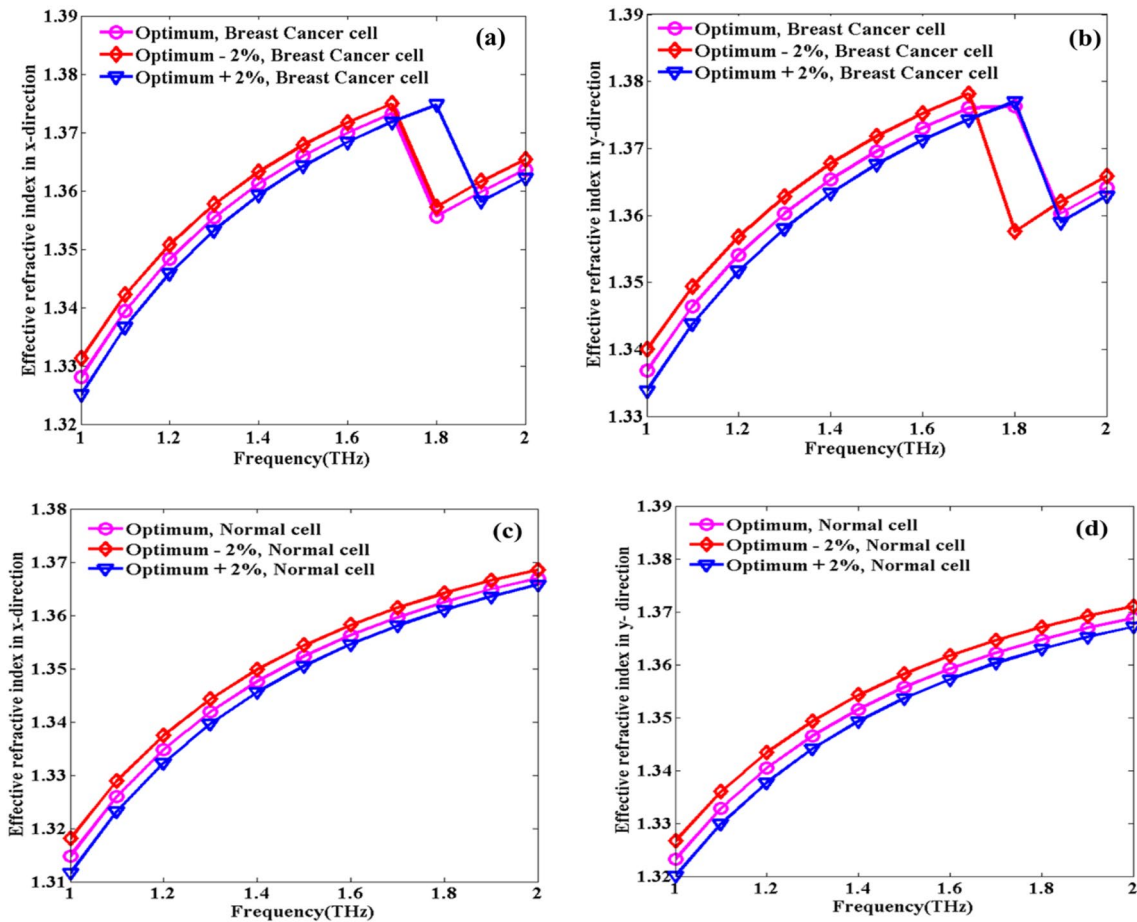


Fig. 7 a and b Effective refractive index in breast cancer cell along x and y-direction. c and d Effective refractive index in normal cell along x-direction and y-direction

Figure 8a, b represents the cancerous cells' and normal cells' power ratio. The cancerous cells' power ratio values are 48.26562, 47.01512 and 16.1884 and normal cells' power ratio values are 44.99257, 28.68942 and 18.20241

for OPT + 2%, OPT and OPT-2% case respectively. Power increases with increasing frequency and get constant at 1.8 THz frequency for breast cancerous cell. Similarly, for

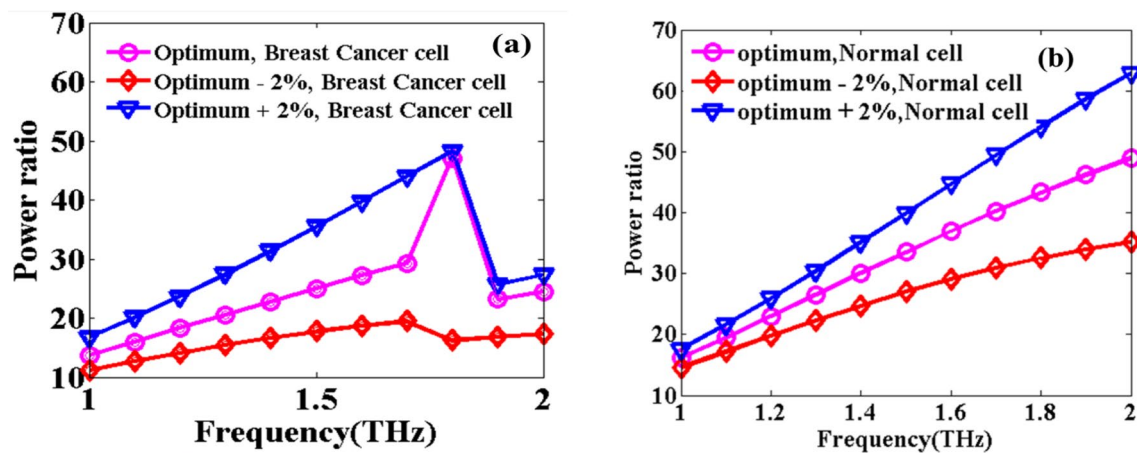


Fig. 8 a Power fraction in breast cancer cell and b normal cell

normal cell, Power increases with increasing frequency and get constant at 1.8 THz frequency.

The variation between power ratio of proposed PCF and the operating frequency is shown in Fig. 8a and b. It has been noticed that PCF’s power fraction increases as frequency rises. At 1.8 THz, the photonic crystal fiber experiences a change in its photonic band structure, leading to an abrupt change in the power ratio. The abrupt decrease in the power ratio is attributed to change in light confinement, resulting in a stronger interaction with the material being sensed. For the propagation mode, the optical power passes through the proposed core, and as frequency rises, light leaks from the core volume to the cladding, causing the progressive attitude [59].

Figure 9a, b and c, d represents the cancerous cells’ relative sensitivity and normal cells’ relative sensitivity, respectively. The cancerous cells’ relative sensitivity values are 65.5347%, 24.5076% and 18.2448% and normal cells’ relative sensitive values are 60.7770%, 48.6416% and 36.5164% for OPT + 2%, OPT and OPT – 2% case, respectively.

With increasing frequency, relative sensitivity increases and becomes constant at 1.8 THz frequency for different cases optimum + 2%, optimum, optimum-2% for breast cancer cell. Similarly, for normal cell with increasing frequency relative sensitivity increases and becomes constant value at 1.8 THz frequency for different cases optimum + 2%, optimum, optimum-2%.

As the input frequency deviates from the system’s resonance frequency, the system’s sensitivity diminishes. However, as the input frequency approaches the system’s resonant frequency, the sensitivity becomes more pronounced, leading to an increase in relative sensitivity. The abrupt change in sensitivity at 1.8 THz is related to the photonic band structure and the existence of resonances within the photonic crystal fiber. At this specific frequency, the sensor experiences a change in the photonic band structure, leading to significant variations in the mode profiles and the interaction of light with the surrounding medium.

The relative sensitivity of the x-polarized mode is always greater than that of the y-polarized mode. It is possibly

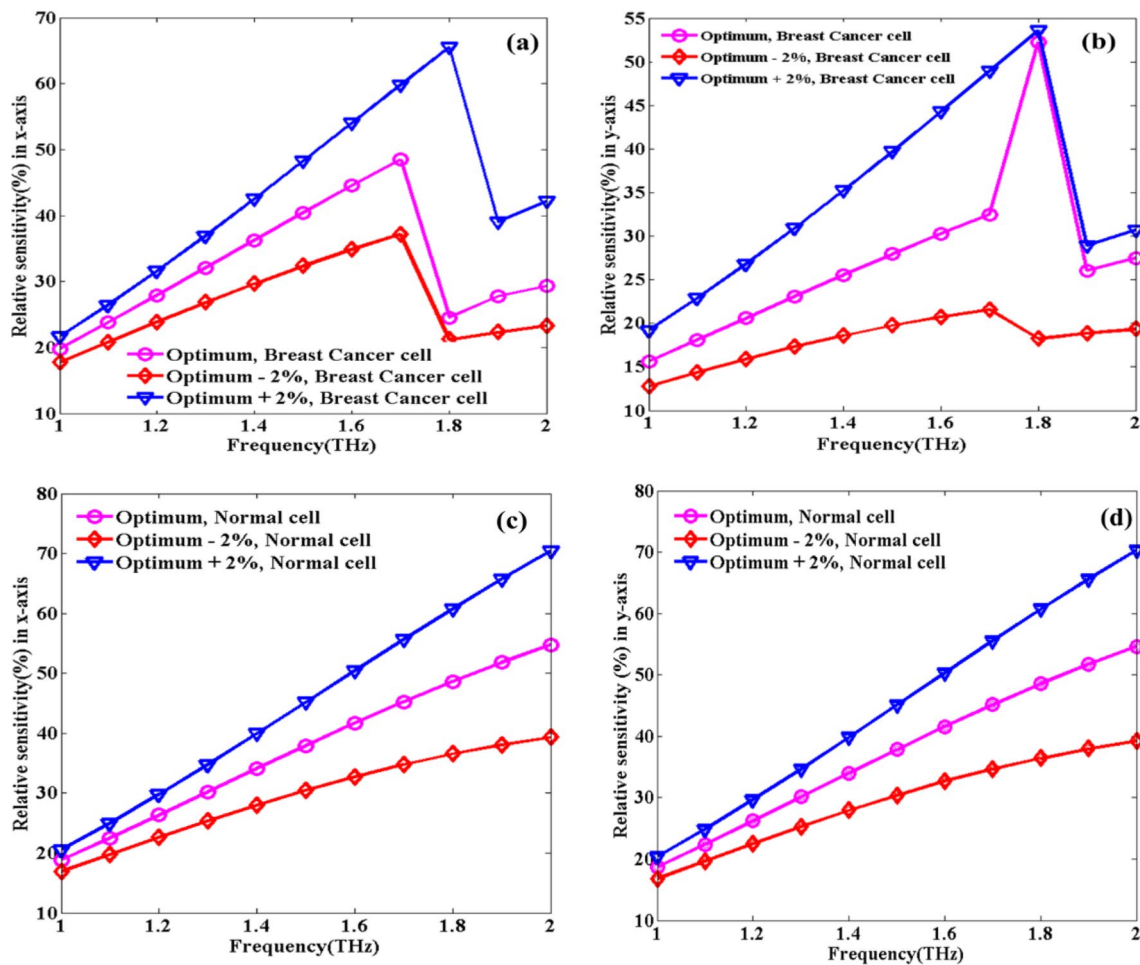


Fig. 9 a Relative sensitivity for breast cancer cell along x-direction and b y-direction and c For normal cell in x-direction d y-direction

because the x-polarized mode has a lower portion of energy distributed outside of the analyte-filling area, such as in strut and the air region in the cladding neighboring the core. Especially, light interacts more strongly with x-polarized mode. So, the x-polarized mode has been selected as the optimum mode for proposed PCF and the characteristics of the x-polarized and y-polarized mode have been exhibited [60].

Figure 10a represents the nonlinearity of the breast cancerous cells and (b) depicts normal cells respectively. The cancerous cells' nonlinear coefficient values are 6.3769×10^{16} , 4.32567×10^{16} , 4.8837×10^{16} and the normal cells' nonlinear coefficient values are 6.1493×10^{16} , 5.5801×10^{16} and 4.9343×10^{16} for OPT + 2%, OPT and OPT - 2% case, respectively. Similarly, both figures demonstrate the variation between nonlinear coefficient and operating frequency of the designed PCF sensor. It is seen that nonlinear coefficient of the PCF increases nonlinearly with increase in frequency.

From Eq. (7), it is evident that nonlinearity has an inverse relation with effective area, which could be seen by comparing Fig. 6a and b. At 1.8 THz, the photonic crystal fiber encounters specific bandgap effects that affect the propagation of light through the fiber. These bandgap effects and resonances leads to changes in the effective refractive index, dispersion properties, and mode interactions. As a result, the nonlinearity exhibits an abrupt change at this frequency, causing it to decrease.

The nonlinear frequency dependence in PCFs is a result of the interaction between light and the material's response at different frequencies. It arises due to complex interactions between the light and the electronic and atomic properties of the medium. At higher frequencies (shorter wavelengths), light carries more energy and interacts more strongly with the material's electrons and atoms.

This increased interaction leads to enhanced nonlinear effects, resulting in a higher nonlinear coefficient at higher frequencies.

Figure 11a shows the breast cancerous cells' dispersion plot and (b) normal cells' dispersion plot. The cancerous cells' dispersion values are 0.1588 ± 0.0121 , 0.1632 ± 0.0113 , 0.1660 ± 0.0241 and the normal cells' dispersion values are 0.1852 ± 0.014 , 5.5801×10^{16} and 4.9343×10^{16} for OPT + 2%, OPT and OPT - 2% case respectively.

From the Eq. (8), it is evident that D relies on the alteration of the effective refractive index. The dispersion variation relies only on the effective refractive index of the waveguide. The obtained dispersion is very small and practically flat, allowing for much easier correlation signal transmission with equivalent pulse expanding. As the effective refractive index varies with frequency, different frequency components of light experience different velocities, leading to group velocity dispersion and affecting the temporal characteristics of light pulses. Understanding and managing dispersion are critical in various optical communication and laser applications to optimize performance and signal integrity.

Table 1 presents the optical characteristics of the proposed PCF based on PbS along with its two variations. This table illustrates that a minor change in structural model throughout fabrication would not result in any issue. Thereby ensure uniform range across all optical parameters but apart from a large degree of variation in the optical characteristics the projected PCF based on PbS is compared to existing PCF based on PbS in Table 2. From Table 2, it is evident that execution of the assumed PbS is finer as analyzed to recently proclaimed PCF-based sensors hence the proposed PCF based on PbS performs exceptionally well in detecting cancerous cells.

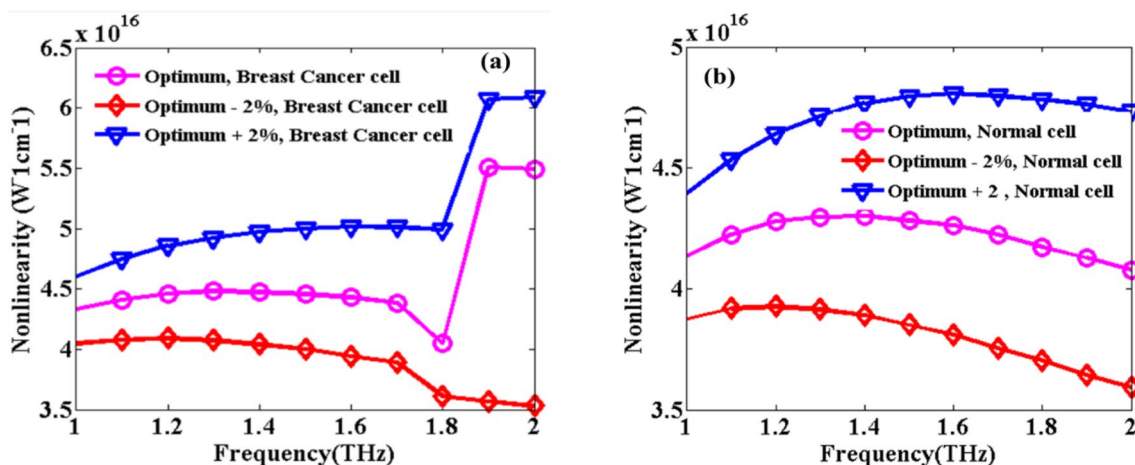


Fig. 10 a Nonlinearity for cancerous cell and b normal cell

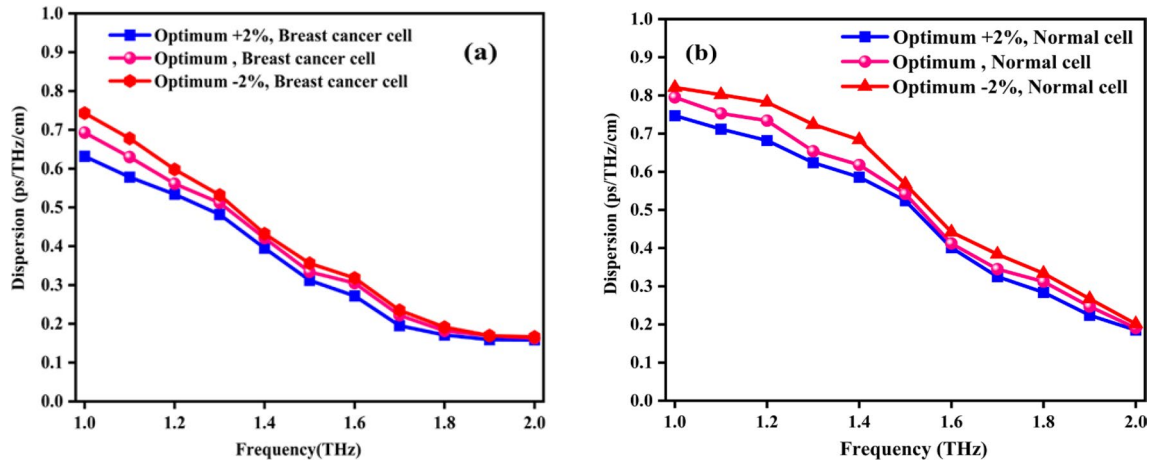


Fig. 11 a Dispersion for the breast cancer cell and b normal cell

Table 2 Performance comparison among different PCF based on PbS

CL (dB/cm)	EA (μm^2)	B	RS (%)	$\gamma(\text{w}^{-1} \text{cm}^{-1})$	D (ps/THz/cm)	n_{eff}	Refs
2.17×10^{-12}	–	0.0051	41.4%	–	–	–	[24]
5.58×10^{-7}	–	0.0080	49.10%	–	–	–	[25]
1.43×10^{-11}	1.61×10^5	–	60.05%	–	–	–	[26]
2.50×10^{-7}	–	–	63.20%	–	–	–	[26]
2.51×10^{-14}	1.44×10^5	–	63.24%	–	–	–	[26]
1.12×10^{-11}	4.40×10^5	–	64.00%	–	–	–	[27]
17.33×10^{-9}	3.04×10^{-8}	0.0020	65.43%	6.377×10^{16}	0.159 ± 0.012	1.3769	(This study)

Conclusion

For optical characteristics accompanying great yielding, the advised photonic crystal fiber sensor for breast cancerous cell identification displays guided treasure. The excellent sensing execution of the studied sensor helps in identifying cancerous cells, which indicates the efficiency and efficacy of the proposed sensor. At frequency range of about 2.0 THz, the electromagnetic field resonate with the specific vibrational modes of the cancer cells or biomolecules, leading to enhance the phenomena of absorption or scattering. Furthermore, the resonant frequency corresponds to the bandgap or photonic crystal mode of the fiber, which affects the transmission or reflection of light. By which the PCF sensor is more applicable in this range to detect the cancer cells. The operating conditions for this PCF sensor model are as follows: the related optical properties at the frequency of 1.8 THz are the best breast cancer sensor models possessing 17.33×10^{-9} dB/cm CL, $3.04 \times 10^{-8} \mu\text{m}^2$ EA and 0.0020 birefringence, effective refractive index 1.376, 65.53% and 53.63% relative sensitivity in the y and x -axes, nonlinearity 6.38×10^{16} , and dispersion 0.1588 ± 0.0121 . Furthermore, the suggested sensor model is fabricable adequately by putting existing

fabrication strategies to the test. Hence the reported sensor a satisfactory candidate for the detection of cancerous cell.

Acknowledgements The first author (Sapana Yadav) expresses gratitude to Madan Mohan Malaviya University of Technology Gorakhpur, India, for financial assistance. Dr. Sachin Singh, Institute of Advanced Materials, IAAM, Sweden and Dr. Yadendra Singh, Boise University, USA have also expressed gratitude for their precious cooperation and assistance.

Funding Not applicable.

Data availability Data will be available made on request.

Declarations

Conflict of interest The corresponding author affirms there is no conflict of interest on representative of all authors.

References

- X.D. Wang, O.S. Wolfbeis, Fiber-optic chemical sensors and biosensors (2008–2012). *Anal Chem* **85**, 487–508 (2013). <https://doi.org/10.1021/ac303159b>

2. F. Wu, P.A. Thomas, V.G. Kravets et al., Layered material platform for surface plasmon resonance biosensing. *Sci Rep* **9**, 1–10 (2019). <https://doi.org/10.1038/s41598-019-56105-7>
3. J.D. Shephard, W.N. MacPherson, R.R.J. Maier et al., Single-mode mid-IR guidance in a hollow-core photonic crystal fiber. *Opt Express* **13**, 7139 (2005). <https://doi.org/10.1364/opex.13.007139>
4. A. Ramola, A. Marwaha, S. Singh, Design and investigation of a dedicated PCF SPR biosensor for CANCER exposure employing external sensing. *Appl. Phys. A Mater. Sci. Process.* **127** (2021). <https://doi.org/10.1007/s00339-021-04785-2>
5. P.J. Roberts, F. Couny, H. Sabert et al., Ultimate low loss of hollow-core photonic crystal fibres. *Opt Express* **13**, 236 (2005). <https://doi.org/10.1364/opex.13.000236>
6. A. Kumar Shakya, S. Singh, Design of novel Penta core PCF SPR RI sensor based on fusion of IMD and EMD techniques for analysis of water and transformer oil. *Meas. J. Int. Meas. Confed.* **188**, 110513 (2022). <https://doi.org/10.1016/j.measurement.2021.110513>
7. S. Yadav, P. Lohia, D.K. Dwivedi, A Novel Approach for Identification of Cancer Cells Using a Photonic Crystal Fiber-Based Sensor in the Terahertz Regime. *Plasmonics* (2023). <https://doi.org/10.1007/s11468-023-01887>. <https://doi.org/10.1007/s11468-023-01887-w>
8. A. Upadhyay, S. Singh, Y.K. Prajapati, R. Tripathi, Numerical analysis of large negative dispersion and highly birefringent photonic crystal fiber. *Optik (Stuttg)* **218**, 164997 (2020). <https://doi.org/10.1016/j.ijleo.2020.164997>
9. K.D. Miller, M. Fidler-Benaoudia, T.H. Keegan et al., Cancer statistics for adolescents and young adults, 2020. *CA Cancer J Clin* **70**, 443–459 (2020). <https://doi.org/10.3322/caac.21637>
10. Y. Ryu, S. Moon, Y. Oh, et al., Effect of coupled graphene oxide on the sensitivity of surface plasmon resonance detection. *Appl. Opt.* **53**, 1419 (2014). <https://doi.org/10.1364/ao.53.001419>
11. Y. Singh, M.K. Paswan, S.K. Raghuvanshi, Sensitivity enhancement of SPR sensor with the black phosphorus and graphene with bi-layer of gold for chemical sensing. *Plasmonics* **16**, 1781–1790 (2021). <https://doi.org/10.1007/s11468-020-01315-3>
12. A.K. Shakya, S. Singh, State of the art alliance of refractive index sensing and spectroscopy techniques for household oils analysis. *Plasmonics* (2023). <https://doi.org/10.1007/s11468-023-01940-8>
13. C.S. Kumar, R. Anbazhagan, Investigation on chalcogenide and silica based photonic crystal fibers with circular and octagonal core. *AEU Int J Electron Commun* **72**, 40–45 (2017). <https://doi.org/10.1016/j.aeue.2016.11.018>
14. P. Kumar, V. Kumar, J.S. Roy, Design of quad core photonic crystal fibers with flattened zero dispersion. *AEU Int J Electron Commun* **98**, 265–272 (2019). <https://doi.org/10.1016/j.aeue.2018.11.014>
15. S. Yadav, S. Singh, P. Lohia et al., Delineation of profoundly birefringent nonlinear photonic crystal fiber in terahertz frequency regime. *J. Opt. Commun.* (2022). <https://doi.org/10.1515/joc-2022-0143>
16. S. Luke, S.K. Sudheer, V.P.M. Pillai, Modeling and analysis of a highly birefringent chalcogenide photonic crystal fiber. *Optik (Stuttg)* **126**, 3529–3532 (2015). <https://doi.org/10.1016/j.ijleo.2015.08.190>
17. A.K. Shakya, S. Singh, Novel Merger of spectroscopy and refractive index sensing for modelling hyper sensitive hexa-slotted plasmonic sensor for transformer oil monitoring in near-infrared region. *Opt Quantum Electron* **55**, 1–25 (2023). <https://doi.org/10.1007/s11082-023-05016-z>
18. Z.H. Tawfiq, M.A. Fakhri, S.A. Adnan, Photonic crystal fibres pcf for different sensors in review. *IOP Conf. Ser. Mater. Sci. Eng.* **454**: (2018). <https://doi.org/10.1088/1757-899X/454/1/012173>
19. A.K. Shakya, S. Singh, Design of a novel refractive index BIO-SENSOR for heavy metal detection from water samples based on fusion of spectroscopy and refractive index sensing. *Optik (Stuttg)* **270**, 169892(2022). <https://doi.org/10.1016/j.ijleo.2022.169892>
20. H. Han, H. Park, M. Cho, J. Kim, Terahertz pulse propagation in a plastic photonic crystal fiber. *Appl Phys Lett* **80**, 2634–2636 (2002). <https://doi.org/10.1063/1.1468897>
21. S. Singh, A.K. Sharma, P. Lohia et al., Design and modelling of high-performance surface plasmon resonance refractive index sensor using BaTiO₃, MXene and nickel hybrid nanostructure. *Plasmonics* **17**, 2049–2062(2022). <https://doi.org/10.1007/s11468-022-01692-x>
22. J. Anthony, R. Leonhardt, A. Argyros, M.C.J. Large, Characterization of a microstructured Zeonex terahertz fiber. *J Opt Soc Am B* **28**, 1013 (2011). <https://doi.org/10.1364/josab.28.001013>
23. Y. Singh, S.K. Raghuvanshi, sensitivity enhancement of the surface plasmon resonance gas sensor with black phosphorus. *IEEE Sensors Lett* **3**, 18–21 (2019). <https://doi.org/10.1109/LSSENS.2019.2954052>
24. M.F.H. Arif, M.M. Hossain, N. Islam, S.M. Khaled, A nonlinear photonic crystal fiber for liquid sensing application with high birefringence and low confinement loss. *Sens. Bio Sens. Res.* **22**, 100252 (2019). <https://doi.org/10.1016/j.sbsr.2018.100252>
25. M.J.B.M. Leon, M.A. Kabir, Design of a liquid sensing photonic crystal fiber with high sensitivity, birefringence and low confinement loss. *Sens. Bio Sens. Res.* **28** 100335(2020). <https://doi.org/10.1016/j.sbsr.2020.100335>
26. M.M. Hasan, S. Sen, M.J. Rana et al., Heptagonal photonic crystal fiber based chemical sensor in THz regime. In: 2019 Jt 8th Int Conf Informatics, Electron Vision, ICIEV 2019 3rd Int Conf Imaging, Vis Pattern Recognition, icIVPR 2019 with Int Conf Act Behav Comput ABC, pp. 40–44(2019). <https://doi.org/10.1109/ICIEV.2019.8858555>
27. I. Yakasai, P.E. Abas, S.F. Kaijage et al., Proposal for a quadrilateral photonic crystal fiber for terahertz wave guidance and sensing chemical warfare liquids. *Photonics* **6** (2019). <https://doi.org/10.3390/photonics6030078>
28. S. Asaduzzaman, M.F.H. Arif, K. Ahmed, P. Dhar, Highly sensitive simple structure circular photonic crystal fiber based chemical sensor. In: 2015 IEEE Int WIE Conf Electr Comput Eng WIECON-ECE 2015 **1**, 151–154 (2016). <https://doi.org/10.1109/WIECON-ECE.2015.7443884>
29. M. De, T.K. Gangopadhyay, V.K. Singh, Prospects of photonic crystal fiber as physical sensor: an overview. *Sensors (Switzerland)* **19**(2019). <https://doi.org/10.3390/s19030464>
30. V.S. Chaudhary, D. Kumar, B.P. Pandey, S. Kumar, advances in photonic crystal fiber-based sensor for detection of physical and biochemical parameters—a review. *IEEE Sens J* **23**, 1012–1023 (2022). <https://doi.org/10.1109/JSEN.2022.3222969>
31. C. Kalyoncu, A. Yasli, H. Ademgil, Machine learning methods for estimating bent photonic crystal fiber based SPR sensor properties. *Heliyon* **8**, e11582(2022). <https://doi.org/10.1016/j.heliyon.2022.e11582>
32. Y. Yi, Y. Ma, S. Wang et al., A new strain sensor based on depth-modulated long-period fiber grating. *Infrared Phys. Technol.* **111**, 103520(2020). <https://doi.org/10.1016/j.infrared.2020.103520>
33. H. Liu, H. Li, Q. Wang et al., Temperature-compensated magnetic field sensor based on surface plasmon resonance and directional resonance coupling in a D-shaped photonic crystal fiber. *Optik (Stuttg)* **158**, 1402–1409 (2018). <https://doi.org/10.1016/j.ijleo.2018.01.033>
34. V.S. Chaudhary, D. Kumar, R. Mishra, S. Sharma, Hybrid dual core photonic crystal fiber as hydrostatic pressure sensor. *Optik (Stuttg)* **210**, 164497(2020). <https://doi.org/10.1016/j.ijleo.2020.164497>
35. L. Zhao, H. Han, Y. Lian et al., Theoretical analysis of all-solid D-type photonic crystal fiber based plasmonic sensor for refractive

- index and temperature sensing. *Opt Fiber Technol* **50**, 165–171 (2019). <https://doi.org/10.1016/j.yofte.2019.03.013>
36. F. Zhang, S. Liu, Y. Wang et al., Highly sensitive torsion sensor based on directional coupling in twisted photonic crystal fiber. *Appl. Phys. Exp.* **11**(2018), <https://doi.org/10.7567/APEX.11.042501>
 37. T. Wang, Y. Mao, B. Liu et al., compact fiber optic sensor for temperature and transverse load measurement based on the parallel vernier effect. *IEEE Photon. J* **14**, 1–8 (2022). <https://doi.org/10.1109/JPHOT.2022.3206313>
 38. N. Ayyanar, G. Thavasi Raja, M. Sharma, D. Sriram Kumar, photonic crystal fiber-based refractive index sensor for early detection of cancer. *IEEE Sens. J.* **18**, 7093–7099(2018). <https://doi.org/10.1109/JSEN.2018.2854375>
 39. A.M. Mairi, P.E. Abas, P.I. Petra et al., Theoretical considerations of photonic crystal fiber with all uniform-sized air holes for liquid sensing. *Photonics* **8**(2021). <https://doi.org/10.3390/photronics8070249>
 40. Z. Liu, F. Sun, C. Wang, H. Tian, Side-coupled nanoscale photonic crystal structure with high-Q and high-stability for simultaneous refractive index and temperature sensing. *J Mod Opt* **66**, 1339–1346 (2019). <https://doi.org/10.1080/09500340.2019.1617444>
 41. S. Sen, M. Abdullah-Al-Shafi, AS Sikder, et al., Zeonex based decagonal photonic crystal fiber (D-PCF) in the terahertz (THz) band for chemical sensing applications. *Sens Bio Sens Res* **31**:100393(2021). <https://doi.org/10.1016/j.sbsr.2020.100393>
 42. M.S. Islam, J. Sultana, M. Faisal et al., A modified hexagonal photonic crystal fiber for terahertz applications. *Opt Mater (Amst)* **79**, 336–339 (2018). <https://doi.org/10.1016/j.optmat.2018.03.054>
 43. C. Wu, B.-O. Guan, C. Lu, H.-Y. Tam, Salinity sensor based on polyimide-coated photonic crystal fiber. *Opt Express* **19**, 20003 (2011). <https://doi.org/10.1364/oe.19.020003>
 44. B. Krishnamoorthi, B. Elizabeth Caroline, M. Michael, S. Thirumaran, A novel rhombic shaped photonic crystal bio-sensor for identifying disorders in the blood samples. *Opt. Quant. Electron* **55**, 1–21(2023). <https://doi.org/10.1007/s11082-023-04584-4>
 45. R. Saha, M.M. Hossain, M.E. Rahaman, H.S. Mondal, Design and analysis of high birefringence and nonlinearity with small confinement loss photonic crystal fiber. *Front Optoelectron* **12**, 165–173 (2019). <https://doi.org/10.1007/s12200-018-0837-6>
 46. M.A. Mollah, M. Yousufali, I.M. Ankan et al., Twin core photonic crystal fiber refractive index sensor for early detection of blood cancer. *Sens. Bio Sens. Res.* **29**, 100344 (2020). <https://doi.org/10.1016/j.sbsr.2020.100344>
 47. X. Yang, C. Shi, D. Wheeler et al., High-sensitivity molecular sensing using hollow-core photonic crystal fiber and surface-enhanced Raman scattering. *J Opt Soc Am A* **27**, 977 (2010). <https://doi.org/10.1364/josaa.27.000977>
 48. A.M.R. Pinto, M. Lopez-Amo, Photonic crystal fibers for sensing applications. *J Sensors* (2012). <https://doi.org/10.1155/2012/598178>
 49. A. Ghazanfari, W. Li, M.C. Leu, G.E. Hilmas, A novel freeform extrusion fabrication process for producing solid ceramic components with uniform layered radiation drying. *Addit Manuf* **15**, 102–112 (2017). <https://doi.org/10.1016/j.addma.2017.04.001>
 50. H. Eboroff-Heidepriem, J. Schuppich, A. Dowler et al., 3D-printed extrusion dies: a versatile approach to optical material processing. *Opt. Mater. Exp.* **4** 1494 (2014). <https://doi.org/10.1364/ome.4.001494>
 51. R.M. Almeida, S. Portal, Photonic band gap structures by sol-gel processing. *Curr Opin Solid State Mater Sci* **7**, 151–157 (2003). [https://doi.org/10.1016/S1359-0286\(03\)00045-7](https://doi.org/10.1016/S1359-0286(03)00045-7)
 52. A.M. Cubillas, S. Unterkofler, T.G. Euser et al., Photonic crystal fibres for chemical sensing and photochemistry. *Chem Soc Rev* **42**, 8629–8648 (2013). <https://doi.org/10.1039/c3cs60128e>
 53. V. Kaur, S. Singh, Extremely sensitive multiple sensing ring PCF sensor for lower indexed chemical detection. *Sens Bio Sensing Res* **15**, 12–16 (2017). <https://doi.org/10.1016/j.sbsr.2017.05.001>
 54. T. Yang, C. Ding, R.W. Ziolkowski, Y.J. Guo, A terahertz (THz) single-polarization-single-mode (SPSM) photonic crystal fiber (PCF). *Materials (Basel)* **12**(2019). <https://doi.org/10.3390/ma12152442>
 55. R.H. Jibon, A.A.M. Bulbul, M.E. Rahaman, Numerical investigation of the optical properties for multiple PCF structures in the THz regime. *Sens. Bio Sens. Res.* **32**, 100405 (2021). <https://doi.org/10.1016/j.sbsr.2021.100405>
 56. M.S. Islam, J. Sultana, K. Ahmed et al., A novel approach for spectroscopic chemical identification using photonic crystal fiber in the terahertz regime. *IEEE Sens J* **18**, 575–582 (2018). <https://doi.org/10.1109/JSEN.2017.2775642>
 57. M.B. Hossain, E. Podder, A.A.M. Bulbul, H.S. Mondal, Bane chemicals detection through photonic crystal fiber in THz regime. *Opt. Fiber Technol.* **54**, 102102 (2020). <https://doi.org/10.1016/j.yofte.2019.102102>
 58. K. Ahmed, F. Ahmed, S. Roy et al., Refractive index-based blood components sensing in terahertz spectrum. *IEEE Sens J* **19**, 3368–3375 (2019). <https://doi.org/10.1109/JSEN.2019.2895166>
 59. M.S. Islam, S. Rana, M.R. Islam et al., Porous core photonic crystal fibre for ultra-low material loss in THz regime. *IET Commun* **10**, 2179–2183 (2016). <https://doi.org/10.1049/iet-com.2016.0227>
 60. B. Fischer, M. Hoffmann, H. Helm et al., Chemical recognition in terahertz time-domain spectroscopy and imaging. *Semicond. Sci. Technol.* **20**(2005). <https://doi.org/10.1088/0268-1242/20/7/015>

Publisher's Note Springer Nature remains neutral with regard to jurisdictional claims in published maps and institutional affiliations.

Springer Nature or its licensor (e.g. a society or other partner) holds exclusive rights to this article under a publishing agreement with the author(s) or other rightsholder(s); author self-archiving of the accepted manuscript version of this article is solely governed by the terms of such publishing agreement and applicable law.